



BIROn - Birkbeck Institutional Research Online

Rogers, M.S.J. and Bithell, M. and Brooks, Sue and Spencer, T. (2021) VEdge_Detector: automated coastal vegetation edge detection using a convolutional neural network. *International Journal of Remote Sensing* 42 (13), pp. 4809-4839. ISSN 0143-1161.

Downloaded from: <https://eprints.bbk.ac.uk/id/eprint/44203/>

Usage Guidelines:

Please refer to usage guidelines at <https://eprints.bbk.ac.uk/policies.html> or alternatively contact lib-eprints@bbk.ac.uk.

1 **VEdge_Detector: Automated coastal vegetation edge detection using a**
2 **convolutional neural network**

3 Martin S. J. Rogers^{a*}, Mike Bithell^a, Susan M. Brooks^b, Tom Spencer^a

4 ^a*Cambridge Coastal Research Unit, Department of Geography, Cambridge University,*
5 *Cambridge, CB2 3EN, United Kingdom.*

6 ^b*Department of Geography, Birkbeck, University of London, Malet Street, London WC1E*
7 *7HX.*

8 Corresponding author*: msjr2@cam.ac.uk

9 Twitter*: @martinsjrogers

10 Research Gate*: Martin_Rogers7

11 Author email addresses: mike.bithell@geog.cam.ac.uk; s.brooks@bbk.ac.uk;
12 ts111@geog.cam.ac.uk

13

14

15

16

17

18

19

20

21

22

23

24

25

26

27

28

29

30 **VEdge_Detector: Automated coastal vegetation edge detection using a** 31 **convolutional neural network**

32 **Abstract**

33 Coastal communities, land covers and intertidal habitats are vulnerable receptors of
34 erosion, flooding or both in combination. This vulnerability is likely to increase with
35 sea level rise and greater storminess over future decadal-scale time periods. The
36 accurate, rapid and wide-scale determination of shoreline position, and its migration, is
37 therefore imperative for future coastal risk adaptation and management. This paper
38 develops and applies an automated tool, VEdge_Detector, to extract the coastal
39 vegetation line from high spatial resolution (Planet's 3 to 5 m) remote sensing imagery,
40 training a very deep convolutional neural network (Holistically-Nested Edge
41 Detection), to predict sequential vegetation line locations on annual to decadal
42 timescales. Red, green and near-infrared (RG-NIR) was found to be the optimum image
43 spectral band combination during neural network training and validation. The
44 VEdge_Detector outputs were compared with vegetation lines derived from ground-
45 referenced positional measurements and manually digitised aerial photographs, which
46 were used to ascertain a mean distance error of < 6 m (two image pixels) and > 84%
47 producer accuracy at six out of the seven sites. Extracting vegetation lines from Planet
48 imagery of the rapidly retreating cliffed coastline at Covehithe, Suffolk, United
49 Kingdom has identified a landward retreat rate > 3 m a⁻¹ (2010 to 2020). Plausible
50 vegetation lines were successfully retrieved from images in The Netherlands and
51 Australia, which were not used to train the neural network; although significant areas of
52 exposed rocky coastline proved to be less well recovered by VEdge_Detector. The
53 method therefore promises the possibility of generalising to estimate retreat of sandy
54 coastlines from Planet imagery in otherwise data-poor areas, which lack ground-
55 referenced measurements. Vegetation line outputs derived from VEdge_Detector are
56 produced rapidly and efficiently compared to more traditional non-automated methods.
57 These outputs also have the potential to inform upon a range of future coastal risk
58 management decisions, incorporating future shoreline change.

59 **Keywords:** Machine learning, automated edge detection, coastal vegetation, satellite
60 imagery, shoreline change analysis.

61

62 1. Introduction

63 Coastal zones are often characterised by high human population densities, presence of critical
64 infrastructure and internationally-designated sites of nature conservation significance. In the
65 **United Kingdom (UK)** alone, damage caused by coastal flooding and erosion frequently
66 exceeds £260 million per year, with the number of properties vulnerable to coastal erosion
67 projected to increase from 9,800 to greater than 100,000 by 2080 (Committee on Climate
68 Change, 2018). Detecting contemporary shoreline position and likely rates of future change is
69 vital for understanding coastal morphological response to changing marine climates and
70 subsequent landscape recovery, and the way these dynamics impact upon human lives and
71 livelihoods. This information is necessary to better inform coastal risk management
72 decisions, including the suitability (or lack thereof) of projected human interventions in the
73 coastal zone (de Andres et al., 2018).

74 Shoreline detection techniques can be broadly categorised into datum-based or proxy-based
75 methods (Pollard et al., 2019a). Datum-based methods use LiDAR (Light Detection And
76 Ranging) or other elevation capture methods (e.g. NextMAP and Terrestrial Laser Scanning)
77 to generate Digital Terrain Models (DTMs) from which the shoreline can be extracted (Brock
78 and Purkis, 2009). From these DTMs, shorelines are commonly delineated as the mean high
79 water (MHW) or other water elevation contour (Moore et al., 2006). Datum-based methods
80 determine both shoreline position and the 3D profile of the coastal zone, but infrequent image
81 capture and inconsistent spatial coverage limit widespread applications (Pardo-Pascual et al.,
82 2018).

83 Proxy-based shoreline analysis can be broadly classified by the use of geomorphological,
84 vegetation, water or human features (Toure et al., 2019), with detection of visibly discernible
85 features through multispectral or panchromatic optical image analysis. The instantaneous

86 waterline position is the dominant shoreline proxy extracted from optical remote sensing
87 imagery (Boak and Turner, 2005). It is commonly delineated by thresholding the Normalised
88 Difference Water Index (NDWI) of a coastal multispectral image (McFeeters, 1996;
89 Hagenaaers et al., 2018) or by conducting land cover classification (Pekel et al., 2016). Using
90 these methods, global, decadal-scale changes in waterline position have been calculated to
91 determine large-scale trends in shoreline position (Luijendijk et al., 2018; Mentaschi et al.,
92 2018). However, collating a time-series of instantaneous water line position in isolation does
93 not necessarily provide an indication of net shoreline migration. The amplitude of horizontal
94 change in waterline position caused by diurnal or semi-diurnal tidal cycles can vary
95 depending on beach gradient, which in turn is often linked to beach sediment size and sorting.
96 So depending on where in the tidal frame the image was captured, tidal range potentially has
97 a greater effect on waterline position than decadal shoreline accretion or erosion (Pugh and
98 Woodworth, 2014). This issue can be mitigated by calculating the mean waterline position
99 extracted from multiple, temporally adjacent, images (Almonacid-Caballer et al., 2016) but
100 this removes the ability to detect short-term variability and, even then, there are spring-neap,
101 equinoctical and nodal tide cycles operating at different timescales. Waterline position can be
102 tidally corrected by considering slope profile and tidal stage during image capture (Vos et al.,
103 2019); although approximate slope profiles have to be used when concurrent datum-based
104 measurements are not available. Thus, given the difficulties of deriving a robust waterline
105 position indicator, there is potential value in seeking out alternative shoreline proxies from
106 remote sensing imagery to quantify temporal rates of shoreline change.

107 The vegetation line is a shoreline proxy which can be flood-responsive, representing the
108 limits to spring high tide flooding, or erosion-responsive, delineating the boundary between
109 the upper beach and the base of sand dunes or soft rock cliffs (Pollard et al., 2019b; Toure et
110 al., 2019). Coastal vegetation lines have been derived through manual digitisation (e.g.

111 Ferreira et al., 2006; Theiler et al., 2013), or by semi-automated methods including
112 thresholding the Normalised Difference Vegetation Index (NDVI, Rahman et al., 2010) and
113 supervised classification of coastal land covers (Zarillo et al., 2008). However, fully
114 automated vegetation line extraction using thresholding and image classification is precluded
115 by variability in the spectral properties of vegetation due to phenology, species, biomass
116 density, vegetation line boundary abruptness, time of year and azimuth. Manual selection of
117 threshold values or class numbers can be time consuming and optimal values can vary within
118 one image. Due to these difficulties, there is a need to investigate the ability of alternative,
119 fully automated methods to extract the vegetation line.

120 Other automated methods used to detect edges in remote sensing imagery can be separated
121 into grey-scale or multispectral edge detectors. Grey-scale edge detection methods include
122 well-established kernel-based methods, including Sobel, Laplacian and Canny edge detection.
123 These single-sized kernels have been used to delimit coastal waterlines as locations with the
124 greatest rate of change in greyscale intensity (Pardo-Pascual et al., 2012; Luijendijk et al.,
125 2018). These methods, however, lose valuable spectral information when converting
126 multispectral imagery to a single band, and they lack the inclusion of semantic information,
127 meaning they may also detect irrelevant boundaries, such as field edges and roads.

128 Machine learning tools, including support vector machines (SVM) and random forests (RF),
129 have been used to classify land covers in multispectral imagery to assist shoreline detection.
130 SVMs maximise the distance between pixels assigned to different classes in feature space
131 (Elnabwy et al., 2020). The coastal waterline has been identified as the boundary between
132 pixels classified by the SVM tool as land or water (Zhang et al., 2013; Elnabwy et al., 2020).
133 Choung and Jo (2017) found the mean error in waterline position to be lower using SVM
134 compared to NDWI thresholding but SVM outputs contained a lot of 'speckle', attributable

135 to the similar spectral properties of shallow water, sand and rock surfaces.

136 RF methods use decision trees to split pixels into subsets with increasingly homogenous pixel
137 values (Breiman et al., 2001). Typically, an ensemble of trees are used, with each individual
138 tree trained using a different sample of the original dataset of pixels. Within each tree, some
139 pixels are withheld during training and subsequently used to validate the accuracy of the
140 classification method (Breiman et al., 2001). Binary land and water maps have been
141 generated using RF (Bayram et al., 2017; Demir et al., 2017) although large mean errors (>
142 22 m) have been recorded between manually digitised shorelines and RF derived shorelines.
143 These differences can be attributed to noise contained within the pansharpened images
144 (Demir et al., 2017). Further, the shallow nature of RF and SVM means they are not robust to
145 identifying spectral-spatial relationships, most saliently that adjacent pixels are likely to
146 belong to the same feature class (Zhang et al. 2016). No applications of RF or SVM to detect
147 the coastal vegetation line could be found in the literature; RF and SVM have only been used
148 to detect the waterline from imagery pertaining to a localised area of interest. Further analysis
149 is necessary to determine whether SVM and RF models, which do not consider the value of
150 neighbouring pixels when classifying a pixel, can be generalised, so as to detect waterline
151 position in other global locations.

152 More recently, Convolutional Neural Networks (CNN) have received increased attention as a
153 way to effectively detect edges in remote sensing imagery. This is in part because they
154 simultaneously consider the value of the pixel of interest and neighbouring pixels (Kokkinos,
155 2016; Zhang et al. 2016). CNNs convolve kernels of different sizes over the raw input image.
156 Smaller kernels (e.g. 3 × 3) capture detailed edge structures but suffer from high incidence of
157 false positives (noise). Conversely, larger kernels detect only the most salient edges,
158 generating blurred boundaries and missing localised detail. Optimal fusing of the outputs

159 from different sized kernels subsequently identifies the most likely location of true edges and
160 minimises noise by considering that edges will be in the same location irrespective of kernel
161 size (Ren, 2008).

162 Holistically-Nested Edge Detection (HED) is an example of a CNN which progressively
163 reduces image resolution, instead of increasing kernel size, to achieve multi-scale image
164 convolution (Xie and Tu, 2015). The HED model architecture contains five separate sets of
165 convolutional layers, all using 3×3 kernels, which are each separated by 2×2 max pooling
166 layers to reduce image resolution. A side output layer is produced after every set of
167 convolutional layers. The first side output contains local boundary detail but is susceptible to
168 noise and false inland boundaries. Conversely, side output 5 only detects salient boundaries
169 and is robust to image noise but the predicted coastal vegetation edge is blurred. These five
170 side output layers are optimally fused to derive the final output, predicting the likelihood of
171 each pixel being an edge (Xie and Tu, 2015; see [Figure 1](#) for a graphical overview of HED
172 architecture).

173 During HED training, every epoch contains a feed forward and back propagation stage.
174 During the feed forward stage, the internal weights in the HED model are used to derive the
175 predicted edge locations from the raw input image. The difference, or loss, between the
176 predicted vegetation line position and the ground-truth binary image is back-propagated
177 through the hidden layers of the HED model, to update the internal HED model weights.
178 These updated weights are subsequently used in the feed forward stage of the next epoch of
179 HED training (see Xie and Tu (2015) and Kokkinos (2016) for a full summary of HED
180 architecture and functionality).

181 Applications of CNN methods, including HED, to detect edges have recently increased in
182 number, due to enhanced computer processing power and greater image availability to train

183 the CNNs e.g. natural image datasets including the Berkeley segmentation dataset (Arbelaez
184 et al. 2007) and ImageNet (Stanford Vision Lab, 2016). The Visual Geometry Group
185 Network (VGGNet-16) model is a CNN with a very similar architecture to HED but contains
186 no side outputs. The model was trained using the ImageNet dataset to detect all objects in
187 natural Red Green Blue (RGB) images e.g. images of animals, humans and everyday items
188 (Simonyan and Zisserman, 2015). Applications of HED to detect every object in natural
189 images are widespread but remote sensing applications, where images contain more noise and
190 a higher density of boundaries, remain highly limited. A key research gap is the retraining
191 and fine tuning of these generalist edge detection CNNs to be able to differentiate between
192 separate types of edge in remote sensing imagery and exclusively extract edges of interest.

193 To exclusively detect particular types of edge in remote sensing imagery, some studies have
194 updated or fine-tuned the weights within pre-existing CNNs by retraining them with remote
195 sensing image pairs. Richer Convolution Networks (RCF), which are CNNs with a similar
196 architecture to HED, have been fine tuned to exclusively detect building boundaries in remote
197 sensing imagery, achieving a higher accuracy than other generalist edge detection algorithms
198 (Lu et al., 2018). Fine tuning was conducted by training the RCF on 1856 image pairs
199 containing an urban scene and a binary image showing building edge and non-edge locations
200 (Lu et al., 2018). Similarly, a U-Net neural network was retrained with Landsat imagery to
201 predict glacial calving front locations (Mohajerani et al., 2019). Remote sensing applications
202 of HED, or modified versions, have been used to detect field boundaries (X.Y. Liu et al.,
203 2019) and to derive land cover classification (X.Y. Liu et al., 2019; Marmanis et al., 2018).
204 H. Liu et al. (2019) modified the standard convolution structure of HED to detect shorelines
205 in heavily urbanised Jiaozhou Bay, China. HED was reported to outperform Sobel and Canny
206 Edge Detection (producer accuracy: Sobel = 0.66, Canny = 0.82, modified HED = 0.95) but
207 no information was provided on the shoreline proxy used. Furthermore, this study trained

208 HED using exclusively RGB spectral bands; further analysis is necessary to identify the
209 optimum spectral band combination during HED training. These abovementioned studies
210 highlight the potential of retraining a CNN to fine-tune its internal weights to exclusively
211 detect a particular type of edge in remote sensing imagery. To date, this approach has not
212 been applied to exclusively detect coastal vegetation edges from remote sensing imagery.

213 This study aims to train and apply a Holistically-Nested Edge Detection (HED) model to
214 extract coastal vegetation lines. The objectives of the paper are to: (i) train a HED model
215 using coastal remote sensing imagery, namely Planet 3 m and 5 m resolution imagery
216 (PlanetScope and RapidEye); (ii) assess the performance of HED in extracting the coastal
217 vegetation line when trained using different combinations of spectral bands as input across a
218 range of coastal settings (Winterton, Suffolk, UK; Perranuthnoe, Cornwall, UK; Bribie
219 Island, Australia and Wilk-Ann-Zee, The Netherlands); (iii) compare Vedge_Detector
220 performance against other experimental methods previously used to detect the coastal
221 vegetation edge, namely ground-referenced measurements and manual digitisation of remote
222 sensing and aerial imagery; and (iv) incorporate the best performing HED model within
223 VEdge_Detector to detect shoreline change from sequential images of Covehithe, Suffolk,
224 UK between 2010 to 2020.

225 *[Image 1 near here]*

226 **2. Materials and Methods**

227 ***2.1. Remote sensing imagery data sources***

228 A total of 78 Planet images (PlanetScope and RapidEye, with 3 and 5 m spatial
229 resolution respectively) were selected for HED training (Planet Team, 2017). Ortho
230 Scene product level imagery was chosen, meaning Planet had orthorectified and
231 radiometrically corrected images prior to image download. Locations were chosen to

232 encompass a diverse range of geomorphic landforms, tidal ranges and vegetation types
233 (see the supplemental material). Training image sizes ranged from 6.3 km² to 1557.5
234 km² and images were selected from all years when Planet imagery was available (2010
235 to 2020). Multiple images were collected from each location to ensure the training
236 dataset contained scenes captured at different tidal stages. This ensured multiple images
237 of the same shoreline, with different beach widths, were contained in the training
238 dataset.

239

240 ***2.2. Holistically-Nested Edge Detection (HED) training***

241 All steps taken in this study were separated into three stages: HED training using coastal
242 remote sensing imagery; validation of the trained HED models; and digital shoreline change
243 analysis using the best performing HED model. The training and validation stages determined
244 the optimal combination of remote sensing spectral bands to train the HED model whilst
245 keeping the HED model architecture constant. The best performing HED model became the
246 VEdge_Detector tool, developed to extract vegetation lines in the shoreline change stage.
247 Figure 2 provides a graphical overview of the three analytical stages.

248 *[Image 2 near here]*

249

250 ***2.2.1. Manual digitisation of the vegetation line***

251 To generate the training dataset, vegetation lines were manually digitised from all 78 training
252 images in ArcGIS 10.5.1. The image NDVI was overlaid at 70% transparency to aid visual
253 vegetation line identification. Where vegetation lines were interrupted, the seaward extent of
254 inland waterbodies or urban areas was used. Vegetation line shapefiles were converted into
255 binary raster edge maps (binary images), with edge pixel values set to 1 and non-edge pixels

256 to 0. Image pairs were subsequently established, containing the original image and the binary
257 image.

258

259 2.2.2 Data Augmentation

260 A large number of images are required during HED training to refine the internal weights
261 within the HED model. Manual digitisation of this number of images would be too time
262 consuming; therefore data augmentation was used to substantially increase training data size
263 from 78 to 10 700 image pairs. Larger images were cropped to size 480×480 pixels (the
264 default image size used by the HED architecture) at multiple locations. The uncropped larger
265 images also formed part of the training dataset, but were resized to 480×480 pixels prior to
266 HED training. Image pairs were flipped vertically, rotated by 90, 180 and 270 degrees and
267 subject to the introduction of Gaussian noise (Figure 3). Gaussian noise was not added to the
268 binary images. Images were rotated around five different points of origin. Image pairs not
269 containing any vegetation line after rotation were automatically discarded. All image pairs
270 were shuffled and randomly assigned into training (80%) and testing (20%) sets prior to CNN
271 input. The proportion of land cover in each image varied from 2% to 98%.

272 *[Image 3 near here]*

273 2.2.3. Holistically-Nested Edge Detection (HED) training

274 HED training was conducted to modify the model's internal weights to increase the model's
275 ability to exclusively detect coastal vegetation edges. To speed up HED training, non-zero
276 weights were initialised prior to training commencement. This study initialised the internal
277 weights contained within the VGGNet-16 architecture prior to training. The weights
278 contained within the VGGNet-16 architecture were derived from training the model on 1.2

279 million natural images to detect everyday objects e.g. animals, people and urban features.
280 Using the weights contained within the VGGNet-16 architecture increased the speed of HED
281 training compared to using randomly assigned weights. The key difference between the
282 architecture in VGGNet-16 and HED is that HED contains side outputs. The side outputs
283 enable deep supervision, whereby every side output is compared to the binary image to
284 calculate loss. By comparison, in VGGNet-16 only the final output is compared to the binary
285 image. Deep supervision guides the neural network to detect transparent objects, i.e. to only
286 detect the edges of objects at a per-pixel level rather than the entirety of an object (Xie and
287 Tu, 2015).

288 To substantiate the assertion that the default weights in the VGGNet-16 architecture were not
289 suitable for detecting exclusively coastal vegetation edges, a HED model containing the
290 default VGGNet-16 weights was used to predict the coastal vegetation edge in an image of
291 Winterton, Suffolk, UK. This HED model failed to detect the coastal vegetation line and
292 instead detected the water line and other inland boundaries (e.g. roads and field edges). This
293 was attributed to the weights in the VGGNet-16 architecture originally being trained to
294 classify all objects in a natural RGB image, whereas the objective of this study is to
295 exclusively extract the vegetation line in remote sensing imagery and discard other
296 boundaries. This reinforced the necessity to retrain the HED model to refine the model
297 weights, using the image pairs derived through manual digitisation and data augmentation.

298

299 During every epoch of HED training, the internal weights in the HED model were used to
300 predict the coastal vegetation line position from the raw image. The class-balanced cross
301 entropy loss function was used to calculate the difference, or loss, between the predicted
302 vegetation line position and the binary image. The loss function was class-balanced to
303 account for the large imbalance between edge and non-edge pixels, i.e. the vast majority of

304 pixels in every image were non-edge. To prevent the HED model from achieving very
305 accurate results if it predicted all pixels to be non-edge, a scaling factor was used. This was
306 calculated by determining the proportion of edge to non-edge pixels in each image. This
307 scaling factor ensured that the HED model was penalised proportionately more for predicting
308 a false negative (predicting an edge pixel to be a non-edge) than a false positive (predicting a
309 non-edge pixel to be an edge).

310 HED model training was implemented in Python's Keras library with Tensorflow backend.
311 The code for the training of HED was modified from Liu (2018) to enable input of 16 bit
312 Planet imagery; selection of the desired image band combination; and the calculation of
313 NDVI. The HED model was run in parallel on four Tesla P100-PCIE-16GB GPUs for 1000
314 epochs, with a running time of seven hours 45 minutes per spectral band combination. The
315 VEdge_Detector tool, instructions and input image specifications are available from GitHub
316 (github.com/MartinSJRogers).

317

318 ***2.3. Validation***

319 The HED model performance was validated by predicting the vegetation line location in
320 seven images not previously seen by the model. All output prediction pixel values ranged
321 between 0 to 1, representing the range in HED confidence that the pixel represented the
322 vegetation line. Confidence contours were used to determine where ground referenced
323 measurements were located in relation to predicted vegetation line confidence curves. HED
324 outputs were accordingly contoured at 0.1 intervals between 0.05 to 0.95 for subsequent
325 model evaluation through comparison with ground-referenced measurements. All contours
326 had a landward and seaward line (see Figure 4 for a demonstration of the vegetation line
327 contours produced).

328 [Image 4 near here]

329 Distance and pixel-based evaluation metrics were used to determine the best performing HED
330 model. Distance-based evaluation of HED performance was conducted by comparing: i)
331 HED model prediction contours (confidence contours) with ground-referenced measurements
332 of vegetation line location; ii) confidence contours to a manually digitised vegetation line of
333 the same image; and iii) ground-referenced measurements to manual digitisation.

334 The ArcMap plugin Digital Shoreline Analysis System (DSAS; (Thieler et al., 2009; USGS,
335 2018)) v5.0 was used in ArcGIS 10.5.1 to calculate distance between shorelines for
336 comparators i), ii) and iii). Distance calculations were made on transects generated at 10 m
337 alongshore intervals, orthogonal to the dominant shoreline orientation. To reduce transect
338 crossing on sinuous coastlines, each transect was drawn orthogonal to a smoothed baseline.
339 This was generated by calculating mean baseline angle over a 200 m interval, with the
340 transect location at the midpoint. Root Mean Square Error (RMSE, Equation (1)) measured
341 the distance between lines. Mean Absolute Error (MAE, Equation (2)) determined net
342 landward (positive) or seaward (negative) bias in prediction contours as shown in the
343 following equations.

344

$$345 \quad \text{RMSE} = \sqrt{\frac{1}{n-1} \sum_{i=1}^n (o_i - p_i)^2} \quad (1)$$

346

347

348

$$349 \quad \text{MAE} = \frac{1}{n} \sum_{i=1}^n |o_i - p_i| \quad (2)$$

350 where o and p are observed and predicted vegetation line positions along each transect, i ,
351 respectively and n is the number of transects. MAE values were assigned as negative if the

352 predicted contours were consistently seaward of the line derived from ground-reference
353 measurements or manual digitisation.

354 The pixel-based evaluation metrics used were user accuracy (Equation (3)), producer
355 accuracy (Equation (4)) and F1 (Equation (5)). All three metrics are suited to classification
356 tasks with imbalance in class populations (e.g. non-edge pixels constitute > 90% of the
357 image),

$$358 \quad U_A = \frac{P_{\text{True}}}{P_{\text{True}} + P_{\text{False}}} \quad (3)$$

359

$$360 \quad P_A = \frac{P_{\text{True}}}{P_{\text{True}} + N_{\text{False}}} \quad (4)$$

361

$$362 \quad F_1 = \frac{P_A \times U_A}{P_A + U_A} \quad (5)$$

363

364 where U_A and P_A are the user accuracy and producer accuracy values respectively. U_A values
365 are more sensitive to the detection of inland non-coastal boundaries, so are typically lower
366 than P_A values. $P_{\text{True}} = \text{True Positive}$ and $N_{\text{True}} = \text{True Negative}$, each corresponding to
367 correctly classified pixels and $P_{\text{False}} = \text{False Positives}$ and $N_{\text{False}} = \text{False Negative}$, each
368 corresponding to incorrectly classified pixels. A pixel incorrectly predicted to be the
369 vegetation line will be classified as a false positive pixel, irrespective of the distance from the
370 manually digitised or ground referenced line. To account for ‘near-misses’, where HED
371 predicts the vegetation line to be at pixels close to the ground-referenced or manual
372 digitisation measurements, the manually digitised and ground referenced lines were buffered
373 to be three pixels wide (instead of one). Relaxed user accuracy, producer accuracy and F_1

374 scores were calculated by comparing HED outputs to the buffered ground referenced and
375 manually digitised vegetation line measurements.

376

377 *2.3.1 Validation image locations*

378 Seven sites were used for HED validation (Table 1). High resolution ground measurements
379 were collected from three of these seven locations along the Suffolk coastline of eastern
380 England on 7 September 2019 (Walberswick, Dunwich and Covehithe) using an RTK-GPS
381 with horizontal positional accuracy of 30 mm. Soft sandy cliffs are located at Covehithe with
382 sharp cliff-top edge vegetation lines. In contrast, a more complex vegetation line on a mixed
383 sand and shingle barrier is present at Walberswick and Dunwich (Pye and Blott, 2006). To
384 ensure at least one ground-referenced measurement per pixel, points were captured
385 approximately every 2 m alongshore and whenever there was a notable change in vegetation
386 line direction. At Dunwich and Covehithe, isolated vegetation patches situated in front of the
387 continuous vegetation line were not demarcated. At Walberswick, two vegetation lines were
388 generated from ground-referenced measurements: i) a landward continuous vegetation line,
389 and ii) locations of isolated seaward vegetation patches. Confidence contours were compared
390 to both vegetation lines derived from ground-referenced measurements at this site.

391 Ground-referenced measurements were compared to HED vegetation line predictions
392 generated from a 3 m resolution PlanetScope image, using distance and pixel-based
393 evaluation metrics outlined above. The PlanetScope image was captured on 12 September
394 2019 and was previously unseen by the HED model. Between 7 and 12 September 2019
395 waves approached from a dominant north easterly direction and rarely exceeded 1 m
396 significant wave height (maximum peak significant wave height at Southwold Approach was
397 1.45 m (Cefas, 2020)). Due to these wave conditions, there is a high degree of confidence that

398 the vegetation line remained stable over this time period.

399 The trained HED model was also used to predict the vegetation line position at four
400 additional locations where ground-referenced measurements were not collected (Table 1). At
401 these locations HED output prediction contours were compared solely to manually digitised
402 vegetation lines. Images from two locations (Winterton, UK and Perranuthnoe, UK) were
403 used during HED training but different image dates were used (training image dates: 2018
404 and 2019, testing image dates: 2010 and 2015). The other two locations were previously
405 unseen by the neural network: Wilk-Ann-See, The Netherlands and a separate section of
406 Bribie Island, Australia.

407 *[Table 1 near here]*

408 ***2.4. Determining the optimum spectral band combination***

409 The default VGGNet-16 weights can only be initialised in a HED model which accepts
410 images with three spectral bands. The performance of the HED model was therefore
411 independently trained using four different combinations of three spectral bands: RGB, RG-
412 NIR, BG-NIR and GB-NDVI. Output predictions from the four HED models were compared
413 to select the most appropriate model for vegetation line detection. Figure 5, 6 & 7 provide a
414 comparison of HED performance using different spectral band combinations at three
415 locations not contained in either the training or validation dataset: Cromer, UK; Varela,
416 Guinea-Bissau and Wyk auf Föhr, Germany. The HED models trained on spectral band
417 combinations RG-NDVI and RGB predicted every pixel in the image to be the coastal
418 vegetation edge, these models were therefore rejected. Only the HED models trained on
419 images with spectral band combinations RG-NIR and BG-NIR were able to discard pixels not
420 pertaining to the coastal vegetation edge. The HED model trained on BG-NIR spectral band
421 images was still unable to discard many non-edge pixels and as a result produced very low

422 user accuracy results of 0.06, 0.02 and 0.02 at Cromer, Varela and Wyk auf Föhr
423 respectively. In contrast, the HED model trained using spectral bands RG-NIR was able to
424 predict the location of the coastal vegetation edge with a user accuracy of 0.26, 0.59 and 0.25
425 at Cromer, Varela and Wyk auf Föhr respectively. The HED model trained using images with
426 RG-NIR spectral bands was thus used to form the basis of the VEdge_Detector tool.

427 *[Image 5 near here]*

428 *[Image 6 near here]*

429 *[Image 7 near here]*

430 **2.5. Shoreline change detection**

431 The VEdge_Detector tool was used to predict the vegetation line from 11 images of
432 Covehithe spanning the period 2010 to 2020. To minimise the influence of seasonal changes
433 to vegetation line location, all selected images were captured in the period between May and
434 August of each year. Confidence contours were generated at 0.1 intervals from 0.05 to 0.95,
435 creating a total of 10 landward and seaward contours per image.

436 Vegetation line change was calculated using DSAS in ArcGIS 10.5.1 (USGS, 2018). The
437 position of the 10 confidence contours for every year was determined along transects running
438 orthogonal to the dominant shoreline direction. Transects were separated by 10 m alongshore
439 intervals. Change in the position of the landward and seaward 0.95, 0.55 and 0.05 confidence
440 contours was calculated to determine rates of vegetation line change. Metrics calculated were
441 Net Shoreline Change (NSC = distance between the oldest and most recent shoreline
442 position) and End Point Rate (EPR = NSC divided by the time interval in years). To minimise
443 geometric errors, ten tie-points were used to ensure consistent georegistration in the 11
444 images used in shoreline change analysis. The locations of stable anthropogenic structures,
445 including road junctions and building corners, were used as the tie points and were

446 distributed evenly over the images.

447 Aerial imagery of Covehithe, provided by the Environment Agency with 10 to 50 cm
448 resolution, was manually digitised (Environment Agency, 2020). NSC values derived using
449 DSAS were compared when using vegetation lines produced by the VEdge_Detector tool and
450 manual digitisation of aerial imagery. Due to aerial imagery availability, NSC values were
451 compared across five baselines: 2010 to 2011, 2013 to 2014, 2015 to 2016, 2016 to 2017 and
452 2017 to 2018.

453

454 3. Results

455 3.1. Manual, ground-referenced and VEdge_Detection measurements

456 Manually digitised vegetation lines were consistently located close to ground-referenced
457 measurements (Root Mean Square Error (RMSE) was 1.72 m, 4.13 m and 2.28 m for
458 Covehithe, Walberswick (landward) and Dunwich respectively). All sites exhibited a
459 landward bias in manual digitisation, with Mean Absolute Error (MAE) of 0.82 m, 3.83 m
460 and 1.83 m respectively. Across all sites, > 93% of transects recorded an error ≤ 2 image
461 pixels (6 m). At Walberswick, where ground-referenced measurements of two vegetation
462 lines were collected, the manually digitised line was located closer to the landward
463 continuous vegetation line than the seaward isolated vegetation patches (manual digitisation
464 to seaward measurements RMSE = 16.72 m and MAE = 13.83 m). VEdge_Detector
465 performance was therefore subsequently compared to the landward ground-referenced
466 measurements at Walberswick.

467 The VEdge_Detector tool extracted continuous vegetation edges at all three field sites (Figure
468 8). For every site the VEdge_Detector 0.95 confidence contours were < 5 m from ground-

469 referenced vegetation line measurements (see Table 2 for summary of all RMSE and MAE
470 values).

471 *[Table 2 near here]*

472 At Walberswick and Covehithe, all ground-referenced measurements were located between
473 or seawards of the 0.95 confidence contours (Figure 8 (a) – (b)). The VEdge_Detector tool
474 performed best at Covehithe with ground-referenced measurements located closest to the
475 seaward 0.95 confidence contour (RMSE = 2.71 m, MAE = -0.02 m). A landward bias in the
476 landward 0.95 contour (MAE = 7.98 m) and a seaward bias in the 0.95 seaward contour
477 demonstrates that ground-referenced measurements at Covehithe were primarily located
478 between the 0.95 confidence contours. Ground-referenced measurements were closest to the
479 seaward 0.05 confidence contour at Walberswick (RMSE = 4.46 m, MAE = -1.11 m). Most
480 ground-referenced measurements were situated between the seaward 0.95 (MAE = 4.31 m)
481 and 0.05 confidence contours. The larger RMSE and MAE values for landward confidence
482 contours compared to seaward contours shows a slight landward bias in VEdge_Detector
483 outputs at Covehithe and Walberswick.

484 The relatively high producer accuracy scores at these two sites (Covehithe = 0.87,
485 Walberswick = 0.84) demonstrate that VEdge_Detector correctly detected a large proportion
486 of vegetation line pixels derived from ground-referenced measurements. However, the lower
487 user accuracy (Covehithe = 0.16 and Walberswick = 0.11) shows that a number of pixels
488 inland of the field derived vegetation line pixels are also being detected by the
489 VEdge_Detector.

490 In contrast to the other two sites, VEdge_Detector predictions were primarily seawards of
491 ground-referenced measurements at Dunwich (0.95 landwards confidence contour RMSE =
492 5.98 m, landward MAE = -5.21 m). The field line was located very close to the 0.05

493 confidence contour (RMSE = 2.37 m, MAE = 1.03 m). Producer accuracy values at Dunwich
494 were consistent with the other two field sites, although a lower user accuracy was recorded
495 (producer accuracy = 0.85, user accuracy = 0.07).

496 *[Image 8 near here]*

497 The VEdge_Detector tool produced a continuous vegetation line at three of the four sites
498 without field data (Figure 9). The tool failed to predict a continuous vegetation line along
499 some cliffed sections at Perranuthnoe, but a continuous line was generated along the beach
500 sections and the cliffed sections to the right of the image (Figure 9 (c)). The tool performed
501 best at Winterton and Bribie Island with errors < 4 m between 0.95 confidence contours and
502 manually digitised lines (Winterton MAE = -3.83 m, Bribie Island MAE = 3.11 m, Figure 9
503 (a) – (b), Table 3). Producer accuracy values > 0.9 were recorded at Winterton, Bribie Island
504 and Wilk-Ann-Zee, demonstrating a very high capability of the tool to detect the manually
505 digitised vegetation line pixels. User accuracy was higher at Bribie (0.39) compared with
506 Winterton (0.11), indicating that the tool produced a less precise line at Winterton.

507 User and producer accuracy values were lower at Wilk-An-Zee and Perranuthnoe (Table 3),
508 although more complex vegetation lines are found at these sites instead of straight sections.

509 More inland pixels were predicted as the vegetation line at these sites (Figure 9 (c) – (d)).

510 There was a greater seaward bias in tool predictions at Perranuthnoe (RMSE = 7.14 m, MAE
511 = -6.63 m), whereas distance-based error at Wilk-Ann-Zee was comparable to Bribie and
512 Winterton (RMSE = 4.61 m, MAE = 5.57 m).

513 *[Table 3 near here]*

514 *[Image 9 near here]*

515 3.2 Digital shoreline change analysis

516 For Covehithe, the VEdge_Detector tool generated confidence curves of vegetation line
517 position from separate images captured in 2010 and 2020 (Figure 10 (a)). A continuous
518 shoreline was extracted from both images, including where the vegetation line is interrupted
519 by the local shingle barriers that enclose Benacre Broad and Covehithe Broad. Total change
520 in shoreline position between these two years was measured using the DSAS tool and the
521 seaward 0.95 confidence contours (Figure 10 (b)). End Point Rates (EPR) along the
522 Covehithe cliffs ranged between 2.47 m a^{-1} and 5.48 m a^{-1} , with an average retreat rate of 3.27
523 m a^{-1} (Figure 10(b)). The total amount of shoreline retreat during this period ranged between
524 24.27 m and 54.38 m; each transect with the smallest and largest retreat are shown as location
525 A and B respectively in Figure 10 (a) – (b). Cross sections of the confidence curves at
526 locations A and B are shown in the two insets in Figure 10 (a). The stretches of shoreline
527 with the greatest rates of retreat corresponded to areas with no overlap in confidence curves.
528 In contrast the confidence curves overlapped up to the 0.2 confidence contours at transects
529 where retreat rates were lower.

530 *[Image 10 near here]*

531 The VEdge_Detector tool was subsequently used to generate confidence curves of vegetation
532 line position at Covehithe annually between 2010 and 2020. Continuous vegetation lines
533 were generated in all years except 2011, 2012 and 2018 when some agricultural fields had
534 been ploughed, leading to apparent breaks in the vegetation line. The relative position of the
535 annual confidence curves from 2010 to 2020 at the location with the fastest rate of retreat is
536 presented in Figure 11. The vegetation line retreated landwards at a faster rate during the first
537 half of the decade (End Point Rate (EPR) 2010 to 2015 = 6.92 m a^{-1} , 2016 to 2020 = 4.31 m
538 a^{-1} , Figure 11). Individual years with the greatest rates of landward retreat were 2010 to 2011

539 (16.1 m ± 3.67 m), 2016 to 2017 (8.80 ± 3.24 m), 2013 to 2014 (6.93 ± 4.20 m) and 2017 to
540 2018 (5.31 ± 3.38 m). The smallest retreat rates were recorded in 2014 to 2015 (1.66 ± 2.45
541 m) and 2018 to 2019 (1.32 ± 3.44 m). The greatest distance between 0.95 landward and
542 seaward confidence contours was in 2013 (6.70 m) and the shortest distance was in 2018
543 (1.23 m).

544 *[Image 11 near here]*

545 Net Shoreline Change (NSC) values derived using DSAS were averaged across the entire
546 Covehithe coastline using both VEdge_Detector 0.95 confidence contours and manual
547 digitisation of aerial imagery. Differences in NSC values obtained using the two methods
548 ranged between 1.31 and 4.19 m, with a mean absolute difference of 2.19 m (Figure 12). An
549 error value of ± 2.71 m was used for VEdge_Detector outputs, the RMSE between
550 VEdge_Detector 0.95 confidence contours and ground-referenced measurements at
551 Covehithe. Errors from digitising aerial imagery were set at 4.76% of each year's NSC value,
552 consistent with calculations of error determined using the same digitisation method in Brooks
553 and Spencer (2010).

554 *[Image 12 near here]*

555 **4. Discussion**

556 *VEdge_Detector performance*

557 VEdge_Detector is the first fully automated tool for the digitisation of the coastal vegetation
558 line from optical remote sensing imagery, where a trained Convolutional Neural Network
559 (CNN) is used to detect the coastal vegetation line. The tool has been adapted from the
560 Holistically-Nested Edge Detection (HED) model (Xie and Tu, 2015), a CNN trained to
561 identify all objects in natural images. Here HED has been retrained to identify exclusively
562 coastal vegetation edges, achieved by training the HED model on a comprehensive set of

563 coastal remote sensing images. At six of the seven validation sites, VEdge_Detector 0.95
564 confidence contours were < 6 m from coastal vegetation edges derived from ground-
565 referenced measurements or manual digitisation of aerial imagery (Table 2 and 3). Previous
566 studies have employed semi-automated methods to detect coastal vegetation, including
567 thresholding and image classification (Zarillo et al., 2008; Rahman et al., 2010).
568 VEdge_Detector advances these studies by being able to identify the coastal vegetation line
569 in isolation, without requiring further post-processing steps to remove inland vegetation land
570 covers and edges.

571 VEdge_Detector differs from other shoreline change studies by exclusively using Planet
572 imagery with 3 m and 5 m spatial resolution. The combined high temporal and spatial
573 resolution and coverage of Planet imagery provides a step-change in the ability to conduct
574 shoreline change analysis. Previous studies have been primarily limited to digitising shoreline
575 position in Google Earth Engine's Landsat or Copernicus imagery with 30 m and 10 m
576 resolution respectively (Gorelick et al., 2017). Improvements in error values when using this
577 imagery have been achieved using soft-classification, contouring and other methods with sub-
578 pixel precision (Foody et al., 2005; Li and Gong, 2016; Pardo-Pascual et al., 2018).
579 Extraction of the coastal vegetation line using imagery with 10 to 30 m resolution will remain
580 problematic as one pixel can span the entire width of the coastal zone, incorporating
581 numerous shoreline proxies. RMSE values derived in this study (2.37 m to 7.97 m) are
582 comparable or a substantial improvement to error values derived from sub-pixel precision
583 methods applied to coarser resolution imagery.

584 The combination of the high (up to daily) temporal resolution of the Planet imagery with the
585 VEdge_Detector tool gives new opportunities to analyse the horizontal change in shoreline
586 position caused by an individual major storm event or a succession of storm events (Roy,

587 2017). Previously this has only been possible through field or aerial based studies (e.g.
588 Spencer et al., 2015). Studies of this nature are rare because data collection methods are time
589 consuming, costly and information on shoreline position and profile prior to the storm event
590 is only available in isolated, data-rich areas. The passive nature of image data collection used
591 in VEdge_Detector, combined with its high spatio-temporal resolution opens new
592 possibilities to assess storm damage, or other discrete erosion or accretion events in relatively
593 understudied or inaccessible areas.

594 VEdge_Detector performed best on relatively simple, straight stretches of shoreline (e.g.
595 Covehithe, Winterton and Bribie Island; Figure 8 (a) – (b)). Perranuthnoe, Cornwall, UK was
596 the only location where VEdge_Detector did not generate a continuous vegetation line. This
597 can be primarily attributed to the additional presence of rocky cliffs, because the majority of
598 training data images contained only beaches. Whilst additional HED training using more
599 images containing rocky cliffed shorelines may improve model performance, this may be at
600 the expense of performance along sandy beached sections. Figure 9 (c) shows that the tool
601 can detect a vegetation line at the base of some of the cliffs at Perranuthnoe, possibly due to
602 the presence of macroalgae on the shore platform. It is beyond the scope of VEdge_Detector
603 to include these sections, because change in macroalgal cover is highly unlikely to reflect an
604 actual landward or seaward migration in shoreline position. Similarly, fixed coastal defences
605 will not contain a mobile vegetation edge. Hence it is important to note that VEdge_Detector
606 is primarily a tool for efficient and rapid extraction of the vegetation line from beach and
607 dune systems over wide spatial coverage, from which shoreline change analysis can be
608 performed.

609 The small discrepancies presented here between manually digitised shorelines and ground-
610 referenced measurements from the first three cases studies provided confidence in using

611 manually digitised shorelines to assess VEdge_Detector performance at several alternative
612 sites where ground-referenced measurement was not possible (RMSE = 1.72 m, 4.13 m and
613 2.28 m for Covehithe, Walberswick (landwards) and Dunwich respectively). At
614 Walberswick, the manually digitised line was closer to the landward field vegetation line
615 measurements, indicating that manual digitisation primarily detects the more continuous
616 vegetation line boundary landwards of the habitat of pioneer species. It appears that the
617 diffuse nature of the vegetation edge in some locations, with isolated, dis-continuous
618 vegetation clumps, can lead to discrepancies between manual digitisation, ground-referenced
619 measurements and VEdge_Detector results because the best available imagery is of 3 to 5 m
620 resolution.

621 This study further showed that the method was robust at detecting the vegetation line on both
622 tropical and temperate coasts. To date, the only previous use of CNNs to extract shoreline
623 position has been limited to a single location (H. Liu et al., 2019). Results presented here for
624 seven different validation sites have shown that at six sites, producer accuracy was above
625 0.85, but user accuracy was lower than producer accuracy at every site (Table 2 and 3). This
626 demonstrates how the tool is competent at correctly predicting the vegetation line pixel
627 derived from ground referenced measurements but also generates a vegetation boundary
628 region instead of a distinct line. These performance metrics are lower than those recorded by
629 H. Liu et al. (2019) (user accuracy = 0.94, producer accuracy = 0.95). However H. Liu et al.
630 (2019) used far coarser spatial resolution imagery (16 m to 50 m) and thus poorer user and
631 producer accuracy results presented here could still result in lower RMSE values. Confidence
632 contours were used throughout this study to determine where ground referenced
633 measurements were located across predicted vegetation line confidence curves. At six of the
634 seven sites, ground referenced measurements were closest to one of the 0.95 confidence
635 contours, with RMSE < 6 m (Figure 8 and 9). This highlights that even though a distinct

636 vegetation line is not predicted, VEdge_Detector commonly predicts the ground referenced
637 vegetation line with higher confidence than the surrounding pixels.

638 Vegetation lines were predicted with higher user accuracy along shorelines with abrupt
639 vegetation edges. The fieldwork and additional validation sites with the highest user accuracy
640 results were Covehithe (user accuracy = 0.16) and Bribie Island (user accuracy = 0.38)
641 respectively. Bribie Island has an abrupt vegetation line as bare sand is found immediately
642 adjacent to eucalyptus forest and Covehithe has an abrupt cliff-top vegetation boundary
643 because cliff line retreat is too rapid for cliff toe vegetation establishment. In comparison,
644 VEdge_Detector user accuracy results were lower at Dunwich (user accuracy = 0.07),
645 Walberswick (user accuracy = 0.11) and Wilk-Ann-Zee (user accuracy = 0.07) which all
646 contain graded psammosere community vegetation on beach dune systems. The low user
647 accuracy and higher producer accuracy results highlight how the vegetation edge is not a true
648 line, but a boundary region graded from no vegetation to increasingly dense vegetation when
649 traversing inland. Discrepancies in the interpretation of vegetation line position occur even
650 when collating ground-referenced measurements. This was demonstrated at Walberswick
651 where producer accuracy increased from 0.59, when using the most seaward pioneer
652 vegetation, to 0.84 when using the landward continuous vegetation edge (Figure 8 (b), Table
653 2). Further investigation, supported with ground-referenced measurements, is required to
654 determine whether this tool not only identifies vegetation edge location but also whether user
655 accuracy results can indicate the degree of abrupt change in a vegetation boundary. An
656 increase in vegetation line ‘abruptness’ can imply a loss of pioneer species seaward of dune
657 systems, perhaps as a result of erosion under storm impacts or wave action associated with
658 particularly high tides. Conversely, increasing widths in vegetation edge can represent
659 relatively stable, or prograding, shoreline locations where vegetation has had the opportunity
660 to establish and migrate seawards.

661 This paper also provides the first-ever comparison of the performance of a HED model using
662 different spectral band combinations. RG-NIR visually outperformed other spectral band
663 combinations, demonstrating the importance of spectral band selection in HED training. This
664 finding is complementary to the universally applied vegetation detection algorithm, NDVI,
665 which utilises the near infrared and red wavebands (Genovese et al., 2001). HED and many
666 other CNN architectures only allow the input of images with three spectral bands (Simonyan
667 and Zisserman, 2015). Improved performance may be achieved by concatenating the outputs
668 of multiple CNNs trained on 3 band images. Marmanis et al. (2018) fused the outputs of two
669 CNNs run in parallel, one CNN trained using spectral band information and the other trained
670 using digital terrain models. Parallel CNNs were reported to automatically classify land
671 covers with 84.8% pixel accuracy, but no comparison to single CNN performance was
672 provided. Further investigations should compare performance of single and multiple parallel
673 CNNs trained exclusively on images with different spectral band combinations.
674

675 *Shoreline change analysis using VEdge_Detector*

676 The VEdge_Detector tool showed predicted a consistent landward shift in vegetation position
677 between 2010 and 2020 at Covehithe, Suffolk (Figure 10). Years when the VEdge_Detector
678 recorded the greatest rates of landward retreat coincide with North Sea storm surge events in
679 December 2013 (Spencer et al., 2015; Wadey et al., 2015) and January 2017 (Floodlist, 2017)
680 and the February to March 2018 ‘Beast from the East’ and ‘mini-Beast’ (Brooks and
681 Spencer, 2019). Average rates of landward retreat at Covehithe derived from
682 VEdge_Detector were consistent with results obtained in this study from manually digitising
683 aerial imagery. The mean difference in NSC values when using VEdge_Detector and
684 digitising aerial imagery was less than one pixel. These NSC values are also complementary
685 to values derived along this stretch of shoreline using other proxy and datum-based methods

686 (Brooks and Spencer, 2012; Burningham and French, 2017). This study has demonstrated the
687 aptitude for the VEdge_Detector tool to accurately and efficiently detect the vegetation line
688 from a relatively data rich shoreline where it has been possible to use other measurements,
689 including aerial imagery, LiDAR data and Ordnance Survey data, to validate precision.
690 Further applications of this tool should investigate its use in relatively data poor regions of
691 the world or in regions where there is a necessity to determine the impact of coastal
692 protection schemes or other anthropogenic interventions in the coastal zone.

693 A continuous vegetation line was generated at Covehithe for eight out of 11 years. During
694 three years the vegetation line was fragmented due to the presence of ploughed agricultural
695 land which interrupted the vegetation line. VEdge_Detector has been shown to be able to
696 overcome issues of vegetation line fragmentation in other images, for example detecting the
697 landward extent of Benacre Broad and Covehithe Broad on the Suffolk coast (Figure 10 (a)).
698 Further studies should increase the ability for the tool to generalise, and use urban and water
699 pixels when the vegetation line is fragmented. Alongside the sometimes fragmented nature
700 of the vegetation line, it may remain an unsuitable proxy to use in shoreline change analysis
701 in circumstances where there have been changes in vegetation communities as a result of both
702 natural and anthropogenic processes unrelated to shoreline position. Therefore, this paper
703 suggests future research should combine multiple shoreline proxies simultaneously to provide
704 a better indication of shoreline change.

705

706 **5. Conclusion**

707 This study has trained a Holistically-Nested Edge Detection (HED) model to produce
708 VEdge_Detector, a fully automated tool for the extraction of coastal vegetation lines along
709 sandy shorelines from optical remote sensing imagery. The semantic knowledge gained

710 during HED training enables VEdge_Detector to discriminate between coastal vegetation
711 edges and other inland vegetation boundaries, thus only extracting the coastal vegetation line
712 and removing the need for subsequent post-processing. VEdge_Detector produces a
713 vegetation confidence curve instead of a discrete line, which better represents how, in reality,
714 the coastal vegetation line is not a distinct boundary but a broad zone where vegetation
715 becomes a more continuous cover when traversing inland. The low error values (RMSE < 6
716 m at all sites) between VEdge_Detector predictions and ground-referenced measurements
717 demonstrates the aptitude for this tool to accurately detect the coastal vegetation edge
718 location. VEdge_Detector performance varied depending on spectral band selection, with red,
719 green and near-infrared shown to be the most pertinent image bands to use for coastal
720 vegetation edge detection. This highlights the importance of image spectral band selection
721 during CNN training in any context.

722 VEdge_Detector has been used to detect a decadal-scale, consistent landward shift in
723 shoreline position at Covehithe, Suffolk, UK. This trend in vegetation line position is
724 consistent with measurements obtained through manually digitising aerial imagery. This
725 exemplifies how using this tool in different locations which exhibit a larger horizontal tidal
726 range, may produce a more robust proxy of shoreline position than using the water line to
727 determine net shoreline change. The Planet imagery used to train the VEdge_Detector tool
728 has sufficient spatio-temporal resolution to investigate the impacts of individual storm events
729 along highly erodible shorelines or human management interventions on shoreline position.
730 The high global coverage of this imagery open news opportunities for shoreline change
731 analysis in otherwise data poor regions of the world.

732

733 **Acknowledgements**

734 The aerial imagery provided is courtesy of the UK Environment Agency. This work was funded
735 through the UKRI NERC/ESRC Data, Risk and Environmental Analytical Methods (DREAM) Centre
736 for Doctorial Training, Grant/Award Number: NE/M009009/1 and is a contribution to UKRI NERC
737 BLUECoast (NE/N015924/1; NE/N015878/1). The authors would like to thank Professor Iris Möller
738 (Trinity College Dublin) for her contributions towards developing the research objective.

739

740

741 **References**

742 Almonacid-Caballer, J., Sánchez-García, E., Pardo-Pascual, J.E., Balaguer-Beser, A.A. and
743 Palomar-Vázquez, J., 2016. Evaluation of annual mean shoreline position deduced
744 from Landsat imagery as a mid-term coastal evolution indicator. *Marine Geology* 372,
745 79–88.

746 Arbelaez, P., Fowlkes, C. and Martin, M. 2007. *The Berkeley Segmentation Dataset and*
747 *Benchmark*. [Online]. Available at: <https://www2.eecs.berkeley.edu/>. [Accessed 13
748 January 2020].

749 Bayram, B., Erdem, F., Akpınar, B., Ince, A.K., Bozkurt, S., Reis, H.C. and Seker, D.Z.,
750 2017. The Efficiency of Random Forest Method for Shoreline Extraction from
751 LANDSAT-8 and GOKTURK-2 Imageries. *ISPRS Annals of the Photogrammetry,*
752 *Remote Sensing and Spatial Information Sciences*, 4, 141-145.

753 Boak, E.H., Turner, I.L., 2005. Shoreline Definition and Detection: A Review. *Journal of*
754 *Coastal Research* 214, 688–703.

755 Breiman, L., 2001. Random forests. *Machine learning*, 45(1), 5-32.

756 Burningham, H. and French, J., 2017. Understanding coastal change using shoreline trend
757 analysis supported by cluster-based segmentation. *Geomorphology* 282, 131-149.

758 Brock, J.C. and Purkis, S.J., 2009. The emerging role of LiDAR remote sensing in coastal
759 research and resource management. *Journal of Coastal Research* 53, 1-5.

760 Brooks, S.M. and Spencer, T., 2010. Temporal and spatial variations in recession rates and
761 sediment release from soft rock cliffs, Suffolk coast, UK. *Geomorphology* 124(1-2),
762 26-41.

763 Brooks, S. and Spencer, T., 2019. Long-term trends, short-term shocks and cliff responses for
764 areas of critical coastal infrastructure. In *Coastal Sediments 2019: Proceedings of the*
765 *9th International Conference* (pp. 1179-1187).

766 Cefas, 2020. *WaveNet interactive map*. [online] Available at: <http://wavenet.cefas.co.uk/Map>
767 [Accessed 21 May 2020].

768 Choung, Y.J. and Jo, M.H., 2017. Comparison between a machine-learning-based method
769 and a water-index-based method for shoreline mapping using a high-resolution
770 satellite image acquired in Hwado Island, South Korea. *Journal of Sensors*, 2017, 1-
771 13.

772 Committee on Climate Change, 2018. *Managing the coast in a changing climate*. Available
773 online: [https://www.theccc.org.uk/publication/managing-the-coast-in-a-changing-](https://www.theccc.org.uk/publication/managing-the-coast-in-a-changing-climate/)
774 [climate/](https://www.theccc.org.uk/publication/managing-the-coast-in-a-changing-climate/) (accessed 14 March 2020).

775 Cowell, P. J., and Thom, B. G. 1994. Morphodynamics of coastal evolution, in: Carter, R. W.
776 G. & Woodroffe, C. D. (Eds), *Coastal evolution, late quaternary shoreline*
777 *morphodynamics*. Cambridge: Cambridge University Press, pp. 33 – 86.

778 de Andrés, M., Barragán, J.M. and Scherer, M., 2018. Urban centres and coastal zone
779 definition: Which area should we manage? *Land use policy* 71, 121-128.

780 Demir, N., Oy, S., Erdem, F., Şeker, D.Z. and Bayram, B., 2017. Integrated shoreline
781 extraction approach with use of Rasat MS and SENTINEL-1A SAR Images. *ISPRS*
782 *Annals of the Photogrammetry, Remote Sensing and Spatial Information Sciences*, 4,
783 445-449.

784 Elnabwy, M.T., Elbeltagi, E., El Banna, M.M., Elshikh, M.M., Motawa, I. and Kaloop, M.R.,
785 2020. An Approach Based on Landsat Images for Shoreline Monitoring to Support
786 Integrated Coastal Management—A Case Study, Ezbet Elborg, Nile Delta,
787 Egypt. *ISPRS International Journal of Geo-Information* 9(4), 199-218.

788 Environment Agency, 2020b. *Vertical Aerial Photography*. Available online:
789 <https://data.gov.uk/dataset>, (accessed 19 June 2020).

790 Ferreira, O., Garcia, T., Matias, A., Taborda, R. and Dias, J.A., 2006. An integrated method
791 for the determination of set-back lines for coastal erosion hazards on sandy
792 shores. *Continental shelf research* 26(9), 1030-1044.

793 Floodlist., 2017. UK – Storm Surge Causes Flooding Along England’s East Coast. Available
794 online: [www.http://floodlist.com/europe/united-kingdom](http://floodlist.com/europe/united-kingdom) (accessed 17 June 2020).

795 Foody, G.M., Muslim, A.M. and Atkinson, P.M., 2005. Super-resolution mapping of the
796 waterline from remotely sensed data. *International Journal of Remote Sensing* 26(24),
797 5381-5392.

798 Genovese, G., Vignolles, C., Nègre, T. and Passera, G., 2001. A methodology for a combined
799 use of normalised difference vegetation index and CORINE land cover data for crop
800 yield monitoring and forecasting. A case study on Spain. *Agronomie* 21 (1), 91-111.

801 Gorelick, N., Hancher, M., Dixon, M., Ilyushchenko, S., Thau, D. and Moore, R., 2017.
802 Google Earth Engine: Planetary-scale geospatial analysis for everyone. *Remote*
803 *Sensing of Environment* 202, 18–27.

804 Hagenaaars, G., de Vries, S., Luijendijk, A.P., de Boer, W.P. and Reniers, A.J., 2018. On the
805 accuracy of automated shoreline detection derived from satellite imagery: A case
806 study of the sand motor mega-scale nourishment. *Coastal Engineering* 133, 113-125.

807 Kokkinos, I., 2015. Pushing the boundaries of boundary detection using deep learning. arXiv
808 preprint arXiv:1511.07386.

809 Li, W. and Gong, P., 2016. Continuous monitoring of coastline dynamics in western Florida
810 with a 30-year time series of Landsat imagery. *Remote Sensing of Environment* 179,
811 196-209.

812 Liu, C (2018). HED: Keras implementation. Github repository <https://github.com/lc82111>.

813 Liu, H., Luo, J., Sun, Y., Xia, L., Wu, W., Yang, H., Hu, X. and Gao, L., 2019. Contour-
814 oriented Cropland Extraction from High Resolution Remote Sensing Imagery Using
815 Richer Convolution Features Network. In 2019 8th International Conference on Agro-
816 Geoinformatics (Agro-Geoinformatics) (pp. 1-6).IEEE.

817 Liu, X.Y., Jia, R.S., Liu, Q.M., Zhao, C.Y. and Sun, H.M., 2019. Coastline Extraction
818 Method Based on Convolutional Neural Networks—A Case Study of Jiaozhou Bay in
819 Qingdao, China. *IEEE Access* 7, 180281-180291.

820 Lu, T., Ming, D., Lin, X., Hong, Z., Bai, X. and Fang, J., 2018. Detecting building edges
821 from high spatial resolution remote sensing imagery using richer convolution features
822 network. *Remote Sensing* 10(9), p.1496- 1515.

823 Luijendijk, A., Hagenaaars, G., Ranasinghe, R., Baart, F., Donchyts, G. and Aarninkhof, S.,
824 2018. The State of the World’s Beaches. *Scientific Reports* 8, 6641.

825 Marmanis, D., Schindler, K., Wegner, J.D., Galliani, S., Datcu, M. and Stilla, U., 2018.
826 Classification with an edge: Improving semantic image segmentation with boundary
827 detection. *ISPRS Journal of Photogrammetry and Remote Sensing* 135, 158-172.

828 McFeeters, S.K., 1996. The use of the Normalized Difference Water Index (NDWI) in the
829 delineation of open water features. *International Journal of Remote Sensing* 17(7),
830 1425-1432.

831 Mentaschi, L., Vousdoukas, M.I., Pekel, J.-F., Voukouvalas, E. and Feyen, L., 2018. Global
832 long-term observations of coastal erosion and accretion. *Scientific Reports* 8, 12876.

833 Mohajerani, Y., Wood, M., Velicogna, I. and Rignot, E., 2019. Detection of glacier calving
834 margins with convolutional neural networks: A case study. *Remote Sensing* 11(1),
835 p.74-87.

836 Moore, L.J., Ruggiero, P. and List, J.H., 2006. Comparing mean high water and high water
837 line shorelines: should proxy-datum offsets be incorporated into shoreline change
838 analysis? *Journal of Coastal Research* 224, 894-905.

839 Pardo-Pascual, J.E., Almonacid-Caballer, J., Ruiz, L.A. and Palomar-Vázquez, J., 2012.
840 Automatic extraction of shorelines from Landsat TM and ETM+ multi-temporal
841 images with subpixel precision. *Remote Sensing of Environment* 123, 1-11.

842 Pardo-Pascual, J.E., Sánchez-García, E., Almonacid-Caballer, J., Palomar-Vázquez, J.M.,
843 Priego De Los Santos, E., Fernández-Sarría, A. and Balaguer-Beser, Á. 2018.
844 Assessing the accuracy of automatically extracted shorelines on microtidal beaches
845 from Landsat 7, Landsat 8 and Sentinel-2 imagery. *Remote Sensing* 10(2), 326- 346.

846 Pekel, J.F., Cottam, A., Gorelick, N. and Belward, A.S., 2016. High-resolution mapping of
847 global surface water and its long-term changes. *Nature* 540(7633), 418-422.

848 Planet Team (2017). Planet Application Program Interface: In Space for Life on Earth. San
849 Francisco, CA. <https://api.planet.com>.

850 Pollard, J. A., Brooks, S.M. and Spencer, T., 2019a. Harmonising topographic & remotely
851 sensed datasets, a reference dataset for shoreline and beach change analysis. *Nature*
852 *Scientific Data* 6(1), 1-42.

853 Pollard, J.A., Spencer, T. and Brooks, S.M., 2019b. The interactive relationship between
854 coastal erosion and flood risk. *Progress in Physical Geography: Earth and*
855 *Environment* 43(4), 574-585.

856 Pugh, D. and Woodworth, P., 2014. Sea-level science: understanding tides, surges, tsunamis
857 and mean sea-level changes. Cambridge University Press.

858 Pye, K. and Blott, S.J., 2006. Coastal processes and morphological change in the Dunwich-
859 Sizewell area, Suffolk, UK. *Journal of Coastal Research* 22(3), 453-473.

860 Rahman, A.F., Dragoni, D. and El-Masri, B., 2011. Response of the Sundarbans coastline to
861 sea level rise and decreased sediment flow: A remote sensing assessment. *Remote*
862 *Sensing of Environment* 115(12), 3121-3128.

863 Ren, X., 2008, October. Multi-scale improves boundary detection in natural images. In
864 European conference on computer vision (pp. 533-545). Springer, Berlin, Heidelberg.

865 Roy, S., 2017. Planet to Google Earth Engine Pipeline (Command Line Interface).

866 Simonyan, K. and Zisserman, A., 2014. Very deep convolutional networks for large-scale
867 image recognition. arXiv preprint arXiv:1409.1556.

868 Spencer, T., Brooks, S.M., Evans, B.R., Tempest, J.A. and Möller, I., 2015. Southern North
869 Sea storm surge event of 5 December 2013: water levels, waves and coastal impacts.
870 *Earth-Science Reviews* 146, 120-145.

871 Stanford Vision Lab, 2016. *ImageNet*. [Online]. Available at <http://www.image-net.org/>.
872 [Accessed 18 November 2019].

873 Thieler, E.R., Himmelstoss, E.A., Zichichi, J.L. and Ergul, A., 2009. Digital Shoreline
874 Analysis System (DSAS) version 4.0 – an ArcGIS extension for calculating shoreline
875 change. US Geological Survey Open-file Report, 2008–1278. US Geological Survey,
876 Reston, VA.

877 Toure, S., Diop, O., Kpalma, K. and Maiga, A.S., 2019. Shoreline Detection using Optical
878 Remote Sensing: A Review. *ISPRS International Journal of Geo-Information* 8, 75.

879 USGS, 2018. Digital Shoreline Analysis System (DSAS).Version 5.0 User Guide. Available
880 online: [https://www.usgs.gov/centers/whcmsc/science/digital-shoreline-analysis-](https://www.usgs.gov/centers/whcmsc/science/digital-shoreline-analysis-system-dsas?qt-science_center_objects=0#qt-science_center_objects)
881 [system-dsas?qt-science_center_objects=0#qt-science_center_objects](https://www.usgs.gov/centers/whcmsc/science/digital-shoreline-analysis-system-dsas?qt-science_center_objects=0#qt-science_center_objects) (accessed 15
882 April 2020).

883 Vos, K., Harley, M.D., Splinter, K.D., Simmons, J.A. and Turner, I.L., 2019. Sub-annual to
884 multi-decadal shoreline variability from publicly available satellite imagery. *Coastal*
885 *Engineering* 150, 160-174.

886 Xie, S. and Tu, Z., 2015. Holistically-nested edge detection. *Proceedings of the IEEE*
887 *International Conference on Computer Vision*, 1395-1403.

888 Wadey, M.P., Haigh, I.D., Nicholls, R.J., Brown, J.M., Horsburgh, K., Carroll, B., Gallop,
889 S.L., Mason, T. and Bradshaw, E., 2015. A comparison of the 31 January – 1
890 February 1953 and 5 – 6 December 2013 coastal flood events around the UK.
891 *Frontiers in Marine Science* 2, 84-111.

892 Zarillo, G.A., Kelley, J., Larson, V., 2008. A GIS Based Tool for Extracting Shoreline
893 Positions from Aerial Imagery (BeachTools) Revised (No. ERDC/CHL-CHETN-IV-
894 73). Engineer research and development center Vicksburg MS coastal and hydraulics
895 lab.

896 Zhang, H., Jiang, Q. and Xu, J., 2013. Coastline Extraction Using Support Vector Machine
897 from Remote Sensing Image. *Journal of Multimedia* 8(2),175-182.

898 Zhang, L., Zhang, L. and Du, B., 2016. Deep Learning for Remote Sensing Data: A
899 Technical Tutorial on the State of the Art. *IEEE Geoscience and Remote Sensing*
900 *Magazine* 4, 22–40.

901

902 **Figure and Table captions**

903

904 Figure 1: Holistically-Nested Edge Detection (HED) architecture. Three spectral bands from
905 every satellite image are selected as HED input. Input images are fed through five distinct
906 stages of image convolution, and between each stage a max pooling layer decreases image
907 size. The squares to the bottom left of the image detail the number of convolution kernels at
908 each stage. The side outputs are resized and optimally fused to generate the output.

909

910 Figure 2: Overview of the three stages carried out in this study. Four Holistically Nested
911 Edge Detection (HED) models were independently trained using different spectral band
912 combinations (training). The performance of each HED model was evaluated using a separate
913 image set (validation). The best performing HED model, trained on images with spectral
914 band combination red, green, near-infrared (RG-NIR), formed the VEdge_Detector tool. This
915 tool detected the vegetation line position from multiple images of the same shoreline captured
916 over a 10 year period (shoreline change detection).

917

918 Figure 3: Transformations used in data augmentation (a) original image (cropped to 480 ×
919 480 pixel size), (b) – (d) original image rotated by 90°, 180° and 270°, (e) original image
920 flipped vertically, (f) – (h) flipped image rotated by 90°, 180° and 270°, (i) – (l) Gaussian
921 noise added to the flipped images. Transformations (b) – (h) were simultaneously conducted
922 on the binary images.

923

924 Figure 4: Example of 0.05 (yellow), 0.55 (orange) and 0.95 (red) confidence contours
925 produced by VEdge_Detector at Winterton, UK. The confidence contours were generated
926 from the raw VEdge_Detector output, which is overlaid as the blue colour ramp. Light and
927 dark blue pixels represent the locations predicted as being an edge pixel with a high and low
928 confidence respectively. The manually digitised vegetation line (black) is displayed for visual
929 comparison. Land and sea are found to the left and right of the image respectively. Aerial
930 imagery, provided by the Environment Agency with 40 cm resolution, is used as a backdrop
931 (Environment Agency, 2020).

932

933 Figure 5: (a) Original 3 m PlanetScope image of Cromer, Norfolk, UK (52°93'58.3 N,
934 1°27'18.0 E). Predicted coastal vegetation edge locations using the HED model trained with
935 spectral band combination (b) RGB, (c) RG-NDVI, (d) BR-NIR, (e) RG-NIR.

936

937 Figure 6: (a) Original 5 m RapidEye image of Varela, Guinea-Bissau (12°28'61.0 N, -
938 16°59'45.7 E). Predicted coastal vegetation edge locations using the HED model trained with
939 spectral band combination (b) RGB, (c) RG-NDVI, (d) BR-NIR, (e) RG-NIR.

940

941 Figure 7: (a) Original 3 m PlanetScope image of the islands of Sylt, Amrum and Föhr, Frisian
942 Islands, Germany (54°68'31.4 N, 8°55'74.4 E). Predicted coastal vegetation edge locations

943 using the HED model trained with spectral band combination (b) RGB, (c) RG-NDVI, (d)
944 BR-NIR, (e) RG-NIR.

945

946 Figure 8: Comparison of VEdge_Detector tool predictions to field measurements of
947 vegetation line at (a) Covehithe, (b) Walberswick and (c) Dunwich. Locations of photograph
948 (a)i, (b)i and (c)i are show by arrows on corresponding images. The solid black lines show
949 the field-delineated vegetation lines at all sites. At Walberswick, the landward and seaward
950 vegetation lines derived from field measurements are denoted by a solid and dashed line
951 respectively.

952

953 Figure 9. VEdge_Detector outputs for (a) Winterton, Suffolk, UK (b) A stretch of Bribie
954 Island, Australia, separate to the locations used for training outlined in the supplemental
955 material (c) Perranuthnoe, Cornwall, UK. The red oval indicates the rocky cliff section where
956 the VEdge_Detector failed to detect cliff top vegetation, (d) Wilk-Ann-zee, Netherlands. (a)
957 and (b) display the predicted vegetation line in red with a confidence ≥ 0.95 . (c) and (d) show
958 examples of all VEdge_Detector outputs prior to applying any confidence thresholding.

959

960 Figure 10: (a) VEdge_Detector outputs for a 2010 (red) and 2020 (purple) image of the
961 Covehithe cliffs, Suffolk. Darker colours represent pixels predicted as the vegetation line
962 with a higher confidence. Inset graphs, comparison of vegetation curves at transects situated
963 at location i (smallest recorded change in shoreline position) and ii (largest recorded retreat in
964 shoreline). Note: The image shows VEdge_Detector outputs with confidence values from
965 0.01 to 1.00, whereas the graphs show values 0.05 to 1.00 because the line graphs
966 substantially 'fan' between 0.01 and 0.05. B) Rates of landward retreat (End Point Rate) at
967 Covehithe between 2010 and 2020.

968

969 Figure 11: Top: Vegetation confidence curve position during years 2010 to 2020 at one
970 transect. Bottom: Representation of vegetation curves as a line. Dots represent locations of
971 the 0.95 confidence contours, vertical lines represent locations of the 0.05 confidence
972 contours. Insets **i and ii**: Transect location and all pixels predicted as the vegetation line with
973 confidence > 0.95 overlaid on the 2020 image. Pixel colour coding by year is consistent with
974 line graphs. Some of the colours are occluded in the image due to overlap.

975

976 Figure 12: Comparison of Net Shoreline Change (NSC) values generated the
977 VEdge_Detector 0.95 confidence contours and manually digitised aerial imagery. The blue
978 dots show annual NSC values for the whole of the Covehithe coastline averaged over all
979 orthogonal transects. The ovals represent the error associated with the two methods. The
980 black line shows the position of the blue dots if there was an exact match between NSC
981 values generated using the two methods.

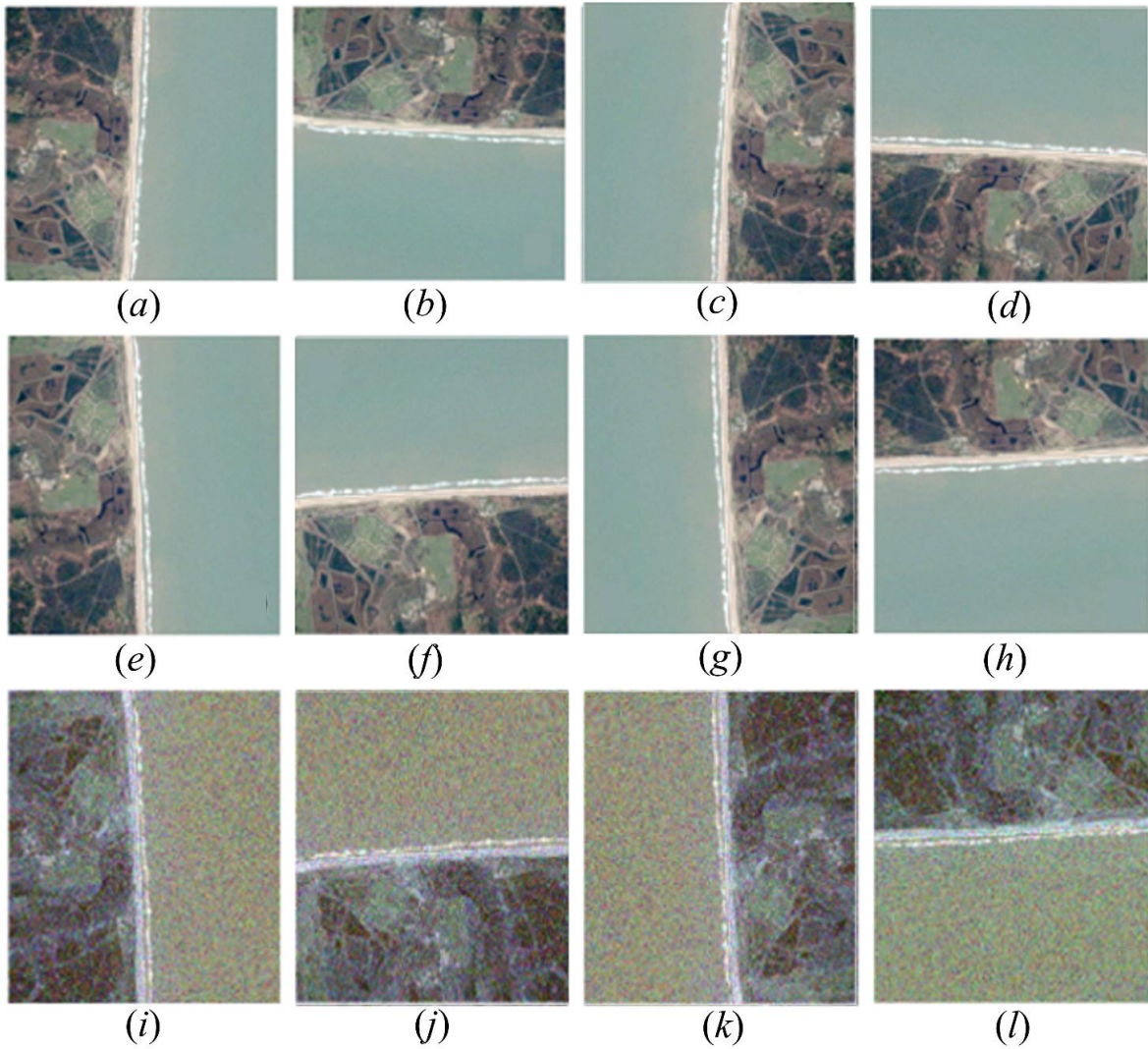
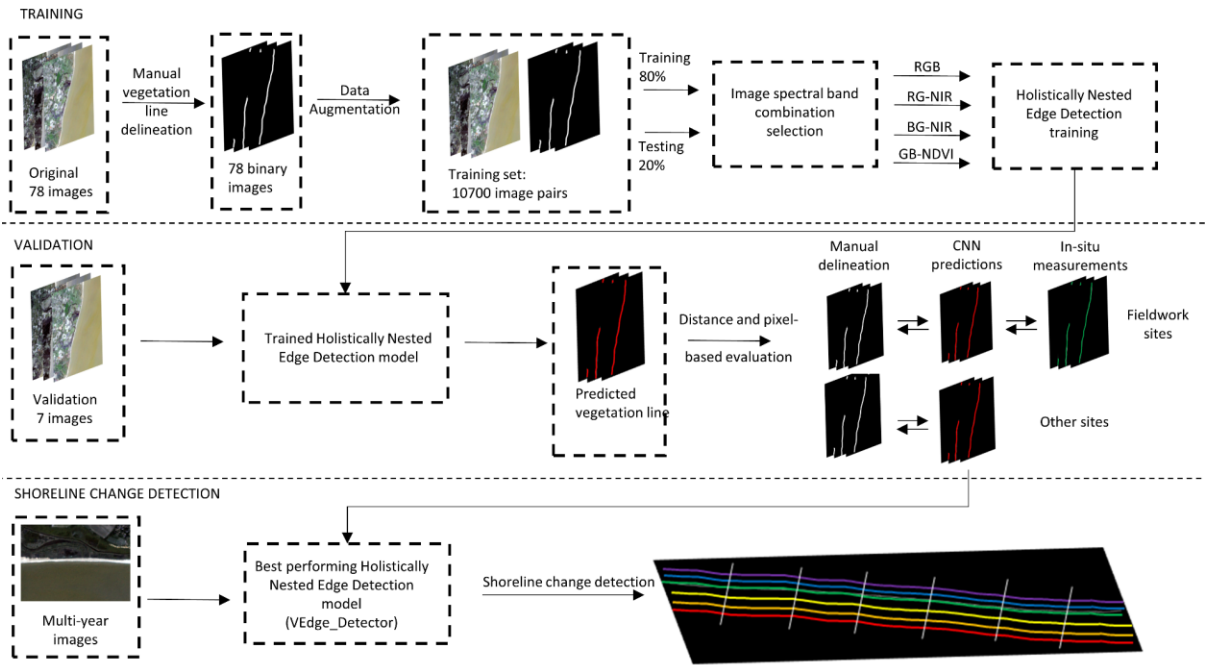
982

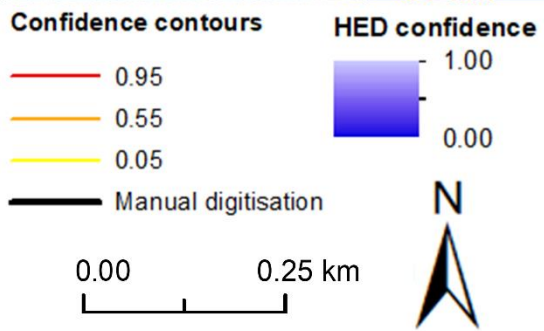
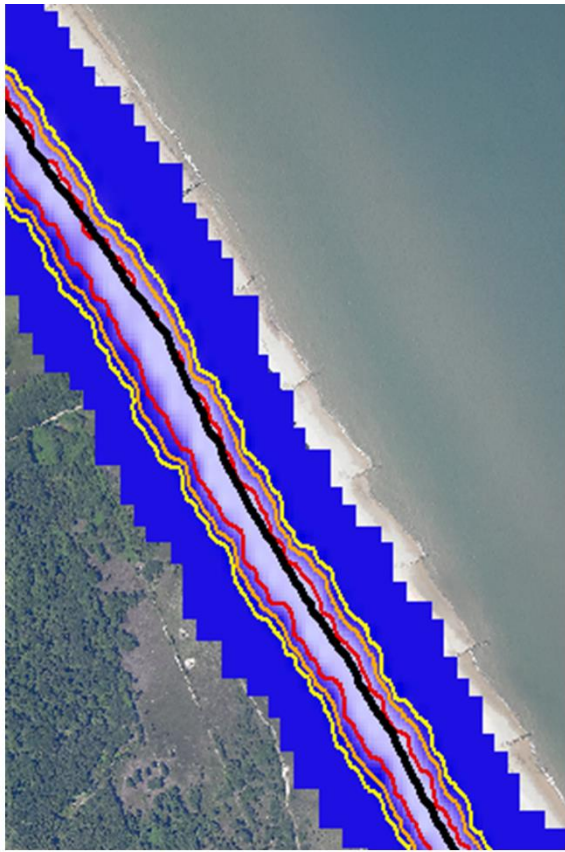
983 Table 1: Locations of Holistically-Nested Edge Detection validation images. Other columns
984 provide information on dominant shoreline direction, spring and neap tidal ranges, dominant
985 sediment type, geomorphology and climate at each site as well as whether ground-referenced
986 measurements of the coastal vegetation edge were collected.

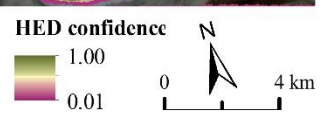
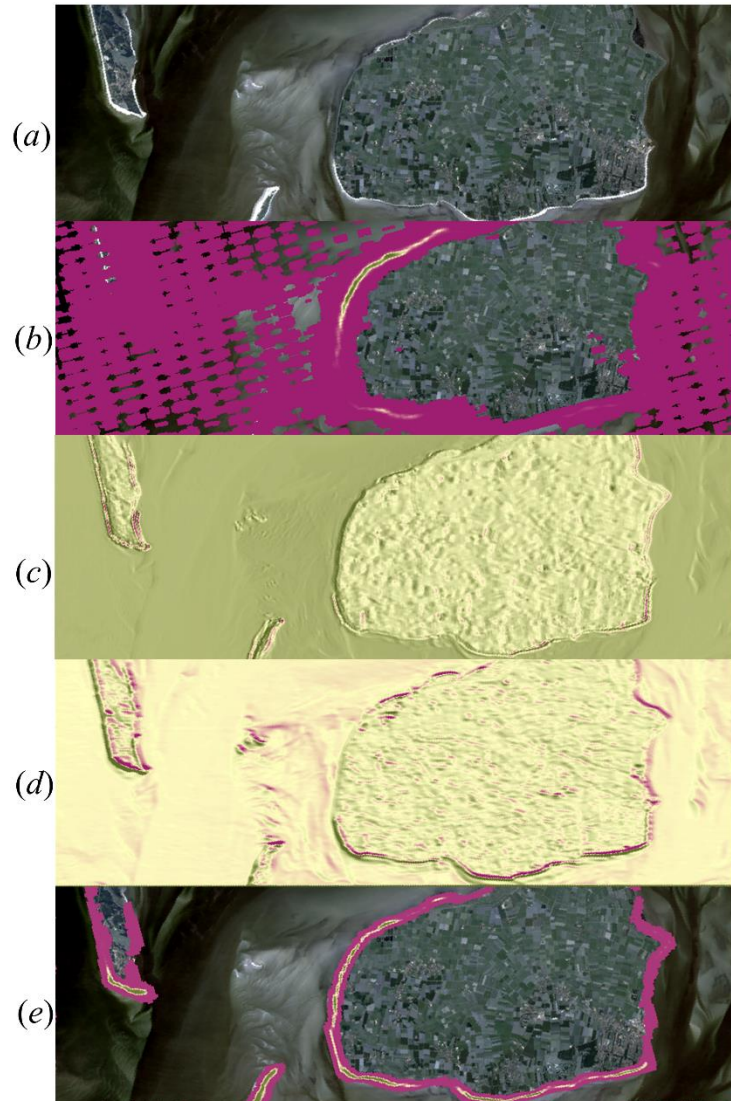
987

988 Table 2: VEdge_Detector accuracy at the three field sites determined by pixel and distance-
989 based metrics from ground-referenced measurements. Shaded pixels in the mean absolute
990 error column represent a landward (green) or seaward (blue) bias respectively in
991 VEdge_Detector predictions. Darker colours represent a greater landward or seaward bias.

992 Red boxes indicate the confidence contours with lowest RMSE and MAE per site.
993 VEdge_Detector outputs are shown in Figure 8.
994
995 Table 3: VEdge_Detector accuracy at the four validation sites without ground-referenced data
996 determined by pixel and distance-based metrics. Shaded pixels in the mean absolute error
997 column represents a landward (green) or seaward (blue) bias respectively in VEdge_Detector
998 predictions. Darker colours represent a greater landward or seaward bias. Red boxes indicate
999 the confidence contours with lowest RMSE and MAE per site. VEdge_Detector outputs are
1000 shown in Figure 9.

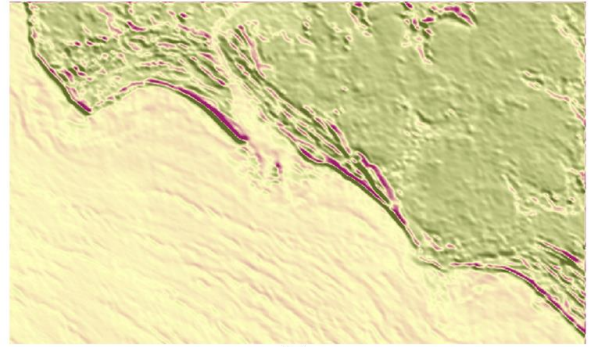








(a)



(b)



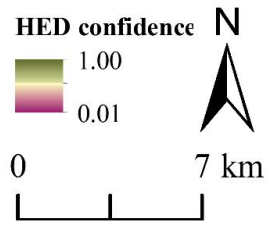
(c)

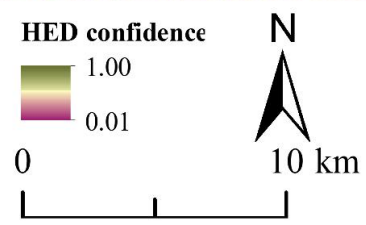
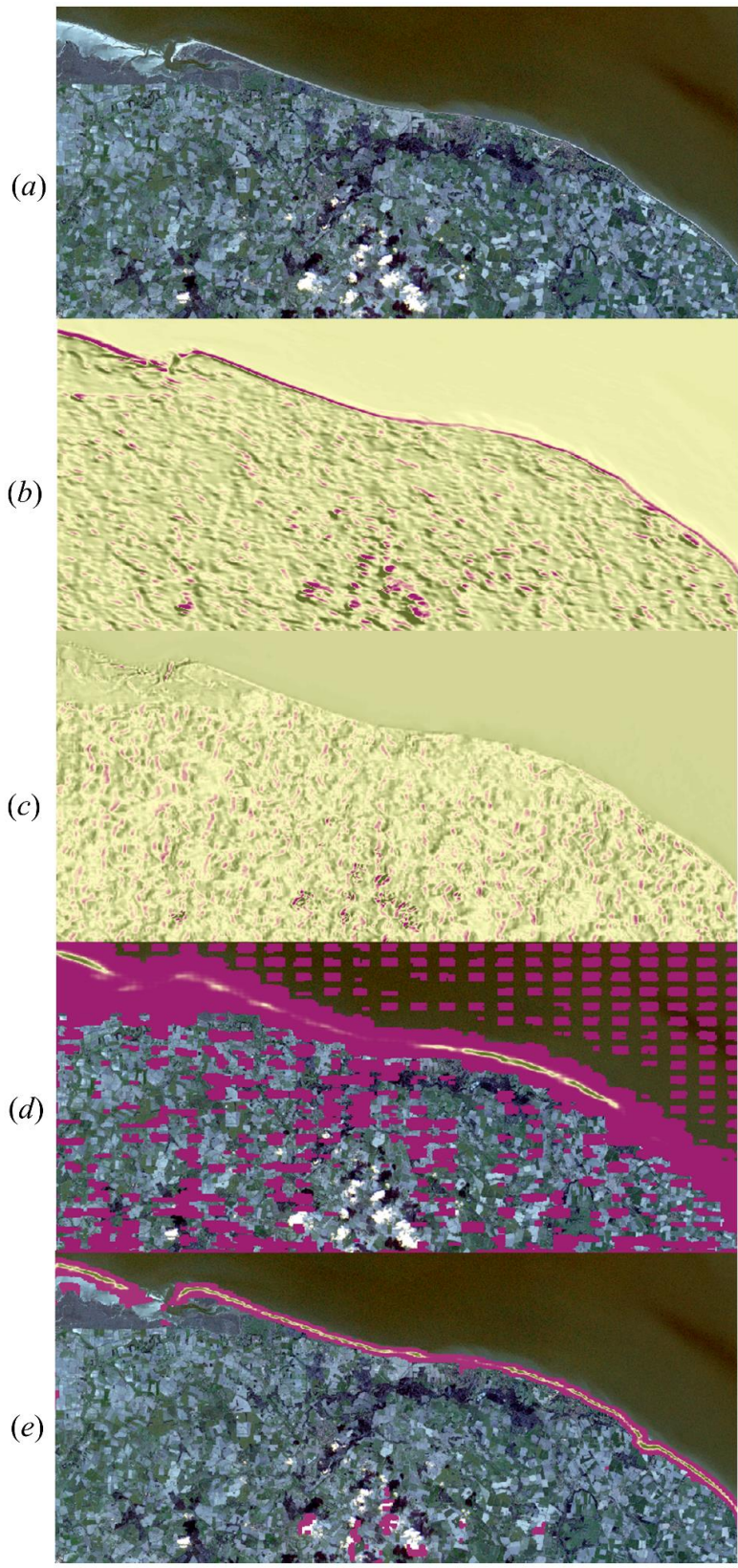


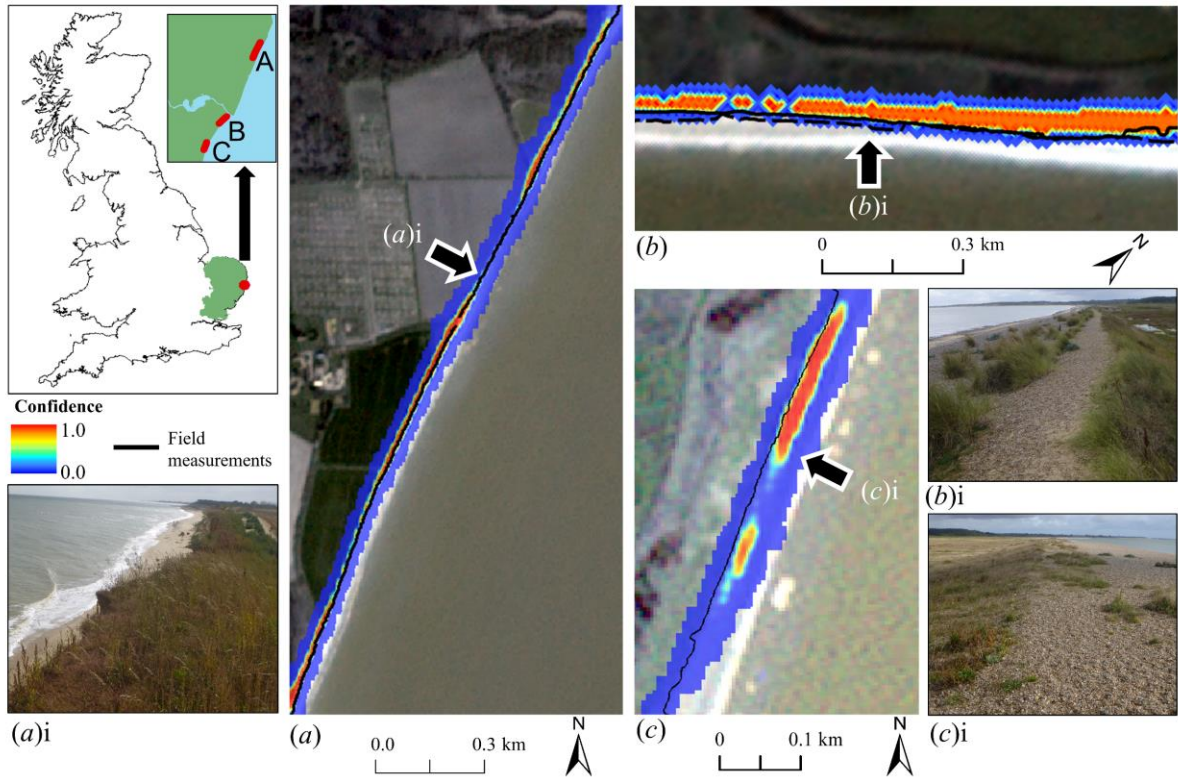
(d)



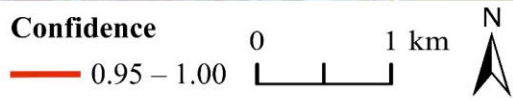
(e)



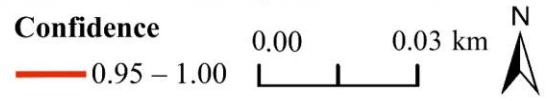
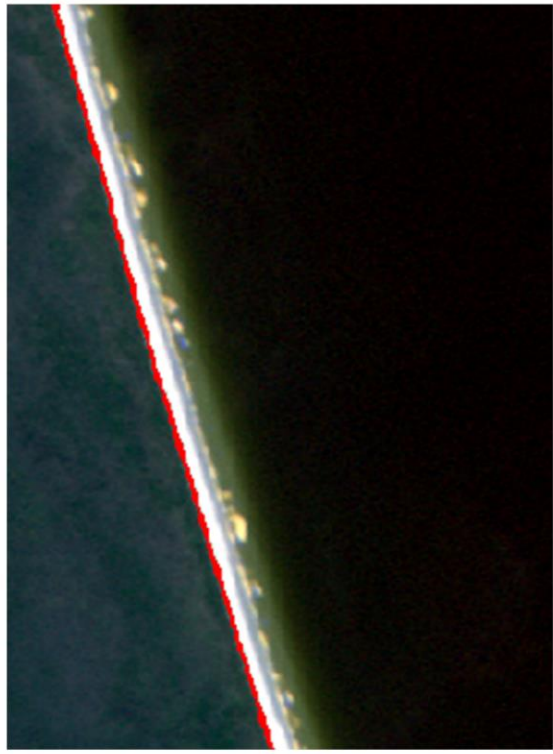




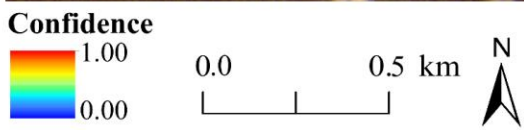
(a)



(b)



(c)



(d)

